

Identifying the Role of Excited-State Proton Transfer and Photoinduced Electron Transfer in Detecting Hypochlorous Acid for a Benzothiazole-Based Colorimetric Fluorescent Probe

Yi Wang (✉ wangyi@dlpu.edu.cn)

Dalian Polytechnic University <https://orcid.org/0000-0002-2042-0980>

Xiumin Liu

Dalian Polytechnic University

Ziming Liu

Dalian Polytechnic University

Research Article

Keywords: colorimetric fluorescent probe, hypochlorous acid, photoinduced electron transfer, ESIPT

Posted Date: March 16th, 2022

DOI: <https://doi.org/10.21203/rs.3.rs-1417982/v1>

License: © ⓘ This work is licensed under a Creative Commons Attribution 4.0 International License.

[Read Full License](#)

Abstract

In this work, the fluorescence mechanism of Hypochlorous Acid (HOCl) chemosensor JBD with 2-(20-Hydroxyphenyl) benzothiazole (HBT) as fluorophore has been investigated by density functional theory (DFT) and time-dependent DFT methods. For JBD probe, the potential energy barrier for the forward excited-state (S_1) intramolecular proton transfer (ESIPT) is 0.71 kcal/mol, while for reversed ESIPT is 8.47 kcal/mol. The stability of Keto isomers provides reliable evidence for the existence of two isomers of JBD in S_1 state. Dual fluorescence of JBD has been observed in the experiment, which is a typical feature for the ESIPT. Through the analysis of the change of intramolecular charge transfer (ICT) extent, it is found that JBD undergo a significant geometric rearrangement upon photoexcitation, which leads to the large Stokes shift. After adding HOCl, the double emission is closed and the fluorescence disappears. We use hole-electrons to analyze the charge distribution, providing evidence for possibility of ICT processes occurring.

Introduction

HOCl, as a kind of biological reactive oxygen species (ROS), plays a key role in the immune defense of invasive pathogens [1-3]. In general, HOCl can be produced in the chemical reaction of H_2O_2 and Cl^- ions mediated by myeloperoxidase (MPO) [4,5]. As an antiseptic germicidal agent, HOCl is common in daily life, such as household bleach, deodorant and disinfectant of swimming pool water [6,7]. Researches have shown that the Chlorine could strongly inactivate novel coronavirus in a short time according to the concentration containing free active chlorine (FAC). However, excessive and abnormal HOCl can cause cardiovascular disease [8], arteriosclerosis [9], and cystic fibrosis [10], and so on [11,12]. Thus, it is necessary to dynamically monitor the activity and small concentration changes of HOCl in living systems, which has become the driving force for the development of various HOCl detection tools.

Numerous probes have been shown to be excellent tools for monitoring HOCl due to their fast response time, high sensitivity, low cost, and multistage fluorescence imaging [13-17]. Moreover, the combination of fluorescent probes and fluorescence imaging can also provide a powerful tool for visualization [18-20]. For example, it has been reported that the photofluorescence imaging of HOCl in lysosomes can be achieved by combining photosoluble protective groups (PPGs) with traditional fluorescent HOCl probe [21]. However, most fluorescent probes are subject to pH-dependence, interference from other ROS and interference from biological fluorescence itself, which impair the applicability of real-time detection of ClO^- . HOCl, as a strong oxidant, can mediate specific reactions of sulfur compounds (S, Se, Te) atoms, Schiff bases, hydrazone and other parts [22,23]. Using the strong oxidation property of HOCl, oxidizable recognition groups such as dibenzoyl hydrazide were selected to undergo fluorescence reaction with HOCl [24]. It also provides ideas for designing more ideal fluorescent probes.

In recent years, more efficient and nondestructive HOCl probes have been explored. In 2021, based on HBT derivatives, a colorimetric fluorescent probe JBD for the detection of HOCl has been synthesized

[25]. In this contribution, HBT acts as an ESIPT-based fluorophore and is linked to pyridine by “C=C” bonds. Moreover, the “C=C” double bond, which serves as the recognition site, is activated by the strongly electron-withdrawing -CN group, resulting in sensitivity to HOCl. Additionally, the ESIPT is realized in this process (Scheme 1). It is worth noting that after adding HOCl, the emission is closed and the fluorescence disappears [25]. Based on the synergistic effect of fluorophore and reaction site, the probe JBD can detect the changes of tiny concentration of intracellular endogenous HOCl with low detection limit and high sensitivity. The physical properties of light and the process of photo-excited electron relaxation are indispensable research contents [26,27]. However, there are still some deficiencies in the study of the physical properties of light in the whole experiment. Moreover, the mechanism of the reaction between fluorophore and HOCl and the mechanism of emission fluorescence are still unclear. Therefore, we theoretically study a detailed and clear ESIPT mechanism and the dynamic process of detecting HOCl. Here, we employ DFT and TD-DFT methods to study the geometrical structure of JBD probe. The theoretical simulations of spectra reproduce the fluorescence phenomena observed in the experiments well. The charge transfer process is studied by hole-electron analysis and the variation of various parameters. Meanwhile, it also provides research ideas for exploring the mechanism of HOCl in oxidative stress and its immune role.

Computational Details

In this paper, all the calculations were carried out using Gaussian 16 program [28]. PBE0/TZVP was selected to serve the calculation [29-31]. The reason is that the functional bearing of Hartree-Fock exchange should not be too high when calculating the vertical transition energies of the excited states. The Hartree-Fock exchange of the PBE0 is relatively low. Moreover, to comply with the previous experiment, the polarizable continuum model (PCM) using the integral equation formalism variant with ACN/H₂O (3:7 v/v) solvent was considered [32-34]. Additionally, we calculated the frequencies of JBD molecule and there exist no imaginary frequencies. What is more, the atom charge was calculated using the Multiwfn program based on the Hirshfeld and Mulliken's charge analysis methods [35-37]. The bond length of O₁-H₂ was increased by a fixed step size, and the potential energy curves (PECs) of the JBD of the S₀ and S₁ states were scanned by PBE0/TZVP level.

Results And Discussion

By adjusting the position of 2-(pyridin-4-yl)propanenitrile (referred to as NP) group, three optimized isomers of probe JBD are obtained in the S₀ state, which are shown in Fig. 1. The dihedral angles of C₁-C₂-C₃-C₄ for JBD-Enol, JBD-Enol-a and JBD-Enol-b structures are 8.9°, 143.7° and -141.1°, respectively. Fig. 2 shows the energy barriers for the torsion of the C₁C₂C₃C₄ dihedral between three isomers in the ground state. The energy of JBD-Enol-b is 0.03 kcal/mol lower than JBD-Enol-a, however, the energy of JBD-Enol is 4.00 kcal/mol lower than JBD-Enol-b. Therefore, the structure JBD-Enol is chosen for the subsequent calculation because of its most stable configuration.

The electron spectra of JBD molecular at TDDFT/PBE0/TZVP level are plotted in Fig. 3. The absorption peak of JBD-Enol is situated at 498 nm, which is comparable with the experiment (493 nm). The -OH group and the =N- group in probe JBD induce proton transfer through Keto-Enol tautomerism. Fig. 3 also shows the fluorescence spectra of JBD-Enol and JBD-Keto in the ACN/H₂O solvent. The main emission bands of JBD-Enol and JBD-Keto are located at 506 and 610 nm, respectively, and the JBD-Keto structure is relatively consistent with the experimental data (607 nm). During ESIPT, JBD-Keto structure becomes the most stable structure, and large Stokes shift (114 nm) is observed for probe JBD.

The results of geometric configurations of JBD-Enol, JBD-Keto, and JBD-open in ACN/H₂O are shown in Fig. 4. The probe JBD has a non-planar structure. As shown in Table 1, the dominant transition of JBD is the S₀→S₁ transition, with the oscillator strength of 0.4697 lying at 498 nm, which is mainly assigned to HOMO→LUMO (87.2%) with smaller components of HOMO-1→LUMO. The FMOs analysis reveals that the HOMO for S₀→S₁ has electron density dispersal over benzothiazole unit, while benzothiazole does not contribute to the LUMO (as shown in Fig. 5). Moreover, the 0.94 electrons transferred signify that the electron excitation of HOMO→LUMO exhibits complete charge transfer (CT) feature. On the other hand, The electron-hole analysis reveals that electron-hole density for S₀→S₂ transition is dispersed over the complete molecular units and the determine the centroid distance (0.86 Å), and their degree of separation (-1.67 Å) indicate the transition as local excitation (LE).

Table 1 Excitation and emission energies of the JBD, including the oscillator strength (*f*) and configuration contributions to the electronic excited states (CI).

	transition	λ(nm/eV)	<i>f</i>	Contribution	CI (%)
JBD-Enol-S ₀	S ₀ →S ₁	498/2.48	0.4697	H→L	87.2
				H-1→L	9.5
	S ₀ →S ₂	435/2.84	0.2745	H-2→L	95.0
	S ₀ →S ₃	425/2.91	0.0421	H-3→L	79.3
				H-1→L	14.5
S ₀ →S ₄	417/2.96	0.0146	H-1→L	51.0	
			H-3→L	19.6	
			H→L+1	17.3	
JBD-Enol-S ₁	S ₁ →S ₀	506/2.45	0.7799	L→H	98.5
JBD-Keto-S ₁	S ₁ →S ₀	610/2.03	0.9325	L→H	99.3

Table 2 The exponent of the for JBD-Enol, including the centroid distance (*D*), the degree of overlap (*S_r*), the width distribution (*H*), degree of separation (*t*), hole delocalization index (HDI) and electron delocalization index (EDI).

	D(Å)	S _r	H(Å)	t(Å)	HDI	EDI	Δr
S ₀ →S ₁	7.21	0.24	2.87	5.09	8.24	7.28	6.80
S ₀ →S ₂	0.86	0.78	4.38	-1.67	5.95	6.19	1.87
S ₁ →S ₀	6.87	0.66	3.42	3.94	7.10	6.90	6.28

Table 3 lists the geometric parameters of JBD-Enol, JBD-Keto and JBD-open. For JBD-Enol, the O₁-H₂ bond length is 0.999 Å in the S₀ state, which increases to 1.033 Å in the S₁ state, growing 0.034 Å; the hydrogen bond length of H₂⋯N₃ decreases from 1.685 Å in the S₀ state to 1.568 Å in the S₁ state. Moreover, the bond angle of O₁-H₂⋯N₃ changes from 147.9° in the S₀ state to 149.6° in the S₁ state, which extends 1.7°. It can be seen that the δ tended to 180° in the S₁ state. These observations indicate that the intramolecular hydrogen bonds become stronger in the S₁ state than that in the S₀ state. Thus, we conclude that enhanced intramolecular hydrogen bonding may be a prerequisite for proton transfer in S₁ state.

The O₁-H₂ bond lengths of JBD-Enol and JBD-open are 0.999 and 0.976 Å, respectively, which verify the formation of hydrogen bond between O₁-H₂ and N₃ in the JBD-Enol form. Additionally, we also constructed the energy curve and shifted the hydroxyl part of the JBD-Enol form by 180° to obtain the JBD-open form, which has non-hydrogen bond (Fig. 6). According to the potential energy curve, JBD-Enol needs to consume 15.02kcal/mol to be converted into JBD-open form. Therefore, it is difficult to form JBD-open structure. Moreover, the electrostatic potential isosurface on the excited state of JBD-Enol is plotted, as shown in Fig. 7. The N₃ atom of JBD exists negative potential value of -16.17 kcal/mol, and the hydrogen atom of H₂-N₃ group has a positive potential value of 3.58kcal/mol. These data suggest that intramolecular proton transfer may occur between such positive and negative sites.

Table 3 Calculated important bond lengths (Å) and bond angles (°) for the optimized structure of JBD-Enol, JBD-Keto and JBD-open in ground-state (S₀) and excited-state (S₁).

JBD-Enol	S ₀	S ₁
O ₁ -H ₂	0.999	1.033
H ₂ -N ₃	1.685	1.568
δ(O ₁ -H ₂ -N ₃)	147.9	149.6
JBD-Keto		
O ₁ -H ₂	1.778	1.857
H ₂ -N ₃	1.044	1.002
δ(O ₁ -H ₂ -N ₃)	133.9	129.2
JBD-open		
O ₁ -H ₂	0.976	1.036
H ₂ -N ₃	3.813	3.816
δ(O ₁ -H ₂ -N ₃)	164.7	171.6

As shown in Fig. 8, the infrared vibration spectra of JBD-Enol and JBD-Keto in the ACN/H₂O solvent have been calculated. For JBD-Enol, the O₁-H₂ peak shifts from 3526 cm⁻¹ in the S₀ state to 3201 cm⁻¹ in the S₁ state. A red shift of 325 cm⁻¹ is observed for the S₁ state, which shows that enhanced hydrogen bonding results in a red shift. For JBD-Keto, the H₂-N₃ peak shifts from 2524 cm⁻¹ in the S₀ state to 3392 cm⁻¹ in the S₁ state. The blue shift of 868 cm⁻¹ is a good reflection of the fact that the O₁⋯H₂-N₃ in JBD-Keto is stronger in the S₀ state than that in the S₁ state.

In addition, Mulliken's charge, Hirshfeld charge and Mayer bond level analysis methods are used to further study the atomic charge distribution in molecules, as shown in Table 4. For JBD-Enol, the negative charges on O₁ that are based on the Mulliken's and Hirshfeld charge analysis change from -0.293 (S₀) to -0.282 (S₁), and -0.204 (S₀) to -0.202 (S₁), respectively. The negative charges of N₃ atom that are based on the Mulliken's and Hirshfeld charge analysis change from -0.123 (S₀) to -0.132 (S₁), and -0.156 (S₀) to -0.172 (S₁), respectively. Generally, the value of Mayer bond level approximates 1.0 for monoatom. If the is close to zero, there is no or almost no bonding existing between two atoms. The Mayer bond levels of two bonds (O₁-H₂ and H₂-N₃) are 0.740 (S₀), 0.727 (S₁) and 0.213 (S₀), 0.212 (S₁), respectively. Above all, the O₁-H₂⋯N₃ hydrogen bond is enhanced in the excited state.

Furthermore, the analysis of FMOs reveals the qualitative representation of electronic charge density (Fig. 9) and it is observed that the HOMO is located at benzothiazole unit, while benzothiazole does not contribute to the LUMO. Thus, HOMO→LUMO transition has the character of ICT and π→π* transitions

for probe JBD. The geometrical relaxation of probe JBD in the S_1 state also reveals the similar behavior. The electron transfer from electron donor to excited fluorophore has strong quenching effect on the fluorophore. Briefly, this fits perfectly with the definition of photoinduced electron transfer (PET) mechanism, which well explains the fluorescence quenching effect. And no fluorescence occurs in the JBD-Enol structure. Additionally, for Keto tautomer, the electron distribution is essentially overlapping. The reactivity can be determined by the energy gap between HOMO and LUMO. As shown in Fig. 9, the E_{gap} values are 3.085 and 2.596 eV in JBD-Enol and JBD-Keto, respectively, which clarify that JBD-Keto has lower kinetic stability and higher chemical reactivity than JBD-Enol. In the S_1 state, the Keto-tautomeric form is stable, and therefore, the emission of probe JBD has resulted from the proton transfer assisted PET phenomena.

Table 4 Calculated Mulliken's charge and Hirshfeld charge of O_1 , H_2 , N_3 atoms; Mayer bond order of O_1 - H_2 and H_2 - N_3 .

	Mulliken's charge			Hirshfeld charge			Mayer bond level	
	O_1	H_2	N_3	O_1	H_2	N_3	O_1 - H_2	H_2 - N_3
S_0	-0.293	0.287	-0.123	-0.204	0.112	-0.156	0.740	0.213
S_1	-0.282	0.311	-0.132	-0.202	0.098	-0.172	0.727	0.212

Fig. 10 shows the PECs along the O_1 - H_2 bond. In the S_0 state, the standard Enol form of probe JBD is more stable than JBD-Keto form (2.97kcal/mol). Thus, after transferring, the structure is unstable, and PT will not occur in the S_0 state. In the S_1 state, at bond length of O_1 - H_2 with 1.778 Å, there is a local minimum. Excited by photoexcitation to the S_1 state, it is JBD-Keto form, which is stabilized by 7.76kcal/mol than JBD-Enol form. It is further proved that the JBD-keto structure becomes the most stable structure in ES IPT process. First, after photoexcitation, JBD-Enol is excited into the form of JBD-Enol* in the S_1 state. The lower energy barrier between the JBD-Enol* and JBD-Keto* forms ensures the ES IPT process.

The stability of Keto isomers provides reliable evidence for the existence of JBD-Keto isomers of JBD in the S_1 state. So, the fluorescence can be emitted by Keto form, which is consistent with the experiment. Additionally, the energies with ZPE of the JBD-Enol, JBD-Keto, and their transition state are also shown in Fig. 11. Adding ZPE correction, the reaction barrier is 2.64kcal/mol in the S_1 state, which provides a strong evidence for the occurrence of ES IPT.

In summary, the fluorescence emission of JBD from Keto form can be well explained by the above theoretical results. Notably, adding HOCl to JBD, a new compound, HBT-COOH, is formed and the fluorescence emission is switched off. HBT-COOH-a structure as the initial structure is carried out the

following research. To investigate the optimal conformation, relaxation scanning of the $N_3C_1C_2C_3$ dihedral was performed, and a rotamer with a $N_3C_1C_2C_3$ dihedral angle of 138° , abbreviated as HBT-COOH-b (Fig. 12c), was obtained. As shown in Fig. 12b, in the S_0 state, the relative energy of HBT-COOH-a is 10.15 kcal/mol lower than that of HBT-COOH-b, indicating that HBT-COOH-a is more stable. By the ground state relaxation scanning the $C_2C_3O_1H_2$ dihedral, a new isomer HBT-COOH-c (Fig. 13c) was obtained. As depicted in Fig. 13b, the HBT-COOH-a is more stable than HBT-COOH-c. Thus, the HBT-COOH-a structure is the optimal conformation.

As shown in Fig. 14, in the S_1 state, after optimization, the proton transfer of HBT-COOH-a could occur spontaneously, and the Keto structure was obtained. Thus, potential energy curves are constructed with a function of O_1-H_2 bond length at PBE0/TZVP level, as depicted in Fig. 15. In the S_0 state, there is no stable point, and PT will not occur in the S_0 state. In the S_1 state, at bond length of O_1-H_2 with 1.124 Å, there is a local minimum. After photoexcitation to the S_1 state, Keto form is stabilized by 8.95 kcal/mol than Enol form, which indicates that the most stable of the HBT-COOH-a molecule should be the Keto structure. Furthermore, in order to explore the reasons for the fluorescence quenching of HBT-COOH-a, in the S_1 state, the torsional potential energy curve of the optimized structure was analyzed. Variation of energy as a function of rotation of the dihedral angle of $N_3-C_1-C_2-C_4$ for transformation of the HBT-COOH-a (S_1) was obtained at the PBE0/TZVP level, as shown in Fig. 16. It is worth noting that the energy of the twisted structure at 90° is significantly higher than the initial energy, which means that the twisted structure is unstable. Thus, the fluorescence quenching of HBT-COOH-a is not caused by the twisted intramolecular charge transfer (TICT). Meanwhile, the FMOs of HBT-COOH-a were analyzed, shown in Fig. 17. The $S_0 \rightarrow S_1$ transition is assigned to HOMO-1 \rightarrow LUMO (98.4%) during the excitation process. The $S_0 \rightarrow S_1$ transition for HBT-COOH-a is a dark state, and its oscillator strength is almost zero (0.0001). This is the main reason for the fluorescence quenching of HBT-COOH-a. Thus, the accuracy of the previous experimental and theoretical results is verified.

Conclusions

In summary, the fluorescence mechanism for a benzothiazole-based colorimetric probe has been researched. In the experiment, the probe JBD has fluorescence emission and a very large Stokes shift in ACN/ H_2O mixed solvent. The theoretical investigation suggests the coupling of the deprotonation in the S_1 state with the disappearance of PET process is responsible for this emission. It is worth noting that after adding HOCl, the emission is closed and the fluorescence disappears. The calculated PEC indicates that HBT-COOH-a needs to overcome a high energy potential barrier to reach the TICT state. It was further verified that the fluorescence quenching of HBT-COOH-a was not caused by TICT. Our work not only strongly confirmed the phenomenon of fluorescence of the probe JBD in the experiment, but also explained the reason for the non-fluorescence of HBT-COOH-a. Therefore, we should further study the

physical and chemical properties of HOCl and design more effective and sensitive probes to monitor the activity capacity of HOCl in the future work.

Declarations

Funding This work was supported by the Open Project of SKLMRD (the open fund of the state key laboratory of molecular reaction dynamics in DICP, CAS) and the General Program from Education department of Liaoning Province (Grant LJKZ0534).

Conflicts of interest The authors declare no competing interest.

Availability of data and material Not applicable

Code availability Not applicable

Authors' contributions The study's conception, design, data collection, analysis, writing, editing, review, and supervision were performed by Yi Wang. The data collection, analysis, writing, editing, and review were performed by Xiumin Liu. The

analysis, review, and editing were performed by Ziming Liu.

References

1. Dickinson BC, Chang CJ (2011) Chemistry and biology of reactive oxygen species in signaling or stress responses. *Nat Chem Biol* 7:504–511
2. Prokopowicz ZM, Arce F, Biedron R, Chiang CLL, Ciszek M, Katz DR, Nowakowska M, Zapotoczny S, Marcinkiewicz J, Chain BM (2010) Hypochlorous acid: a natural adjuvant that facilitates antigen processing, cross-priming, and the induction of adaptive immunity. *J Immunol* 184:824–835
3. Winter J, Ilbert M, Graf PCF, O'zcelik D, Jakob U (2008) Bleach activates a redox-regulated chaperone by oxidative protein unfolding. *Cell* 135:691–701
4. Zhang YR, Meng N, Miao JY, Zhao BX (2015) A Ratiometric Fluorescent Probe Based on a Through-Bond Energy Transfer (TBET) System for Imaging HOCl in Living Cells. *Chem Eur J* 21:19058–19063
5. Zhu B, Wu L, Zhang M, Wang Y, Liu C, Wang Z, Duan Q, Jia P (2018) A highly specific and ultrasensitive near-infrared fluorescent probe for imaging basal hypochlorite in the mitochondria of living cells. *Biosens Bioelectron* 107:218–223
6. Manna A, Goswami S (2015) Ratiometric detection of hypochlorite applying the restriction to 2-way ES IPT: simple design for “naked-eye” tap water analysis. *New J Chem* 39: 4424–4429
7. Wang Y, Xia J, Han J, Bao X, Li Y, Tang X, Ni L, Wang L, Gao M (2016) A fast-responsive fluorescent probe based on BODIPY dye for sensitive detection of hypochlorite and its application in real water samples. *Talanta* 161: 847–853

8. Hazell LJ, Arnold L, Flowers D, Waeg G, Malle E, Stocker R (1996) Presence of hypochlorite-modified proteins in human atherosclerotic lesions. *J Clin Invest* 97:1535–1544
9. Lou Z, Li P, Song P, Han K (2013) Ratiometric fluorescence imaging of cellular hypochlorous acid based on heptamethine cyanine dyes. *Analyst* 138:6291–6295
10. Steinbeck MJ, Nesti LJ, Sharkey PF, Parvizi J (2007) Myeloperoxidase and chlorinated peptides in osteoarthritis: potential biomarkers of the disease. *J Orthop Res* 25:1128–1135
11. Yap YW, Whiteman M, Bay BH, Li Y, Sheu FS, Qi RZ, Tan CH, Cheung NS (2006) Hypochlorous acid induces apoptosis of cultured cortical neurons through activation of calpains and rupture of lysosomes. *J Neurochem* 98: 1597–1609
12. Gungor N, Knaapen AM, Munnia A, Peluso M, Haenen GR, Chiu RK, Godschalk RWL, van Schooten FJ (2010) Genotoxic effects of neutrophils and hypochlorous acid. *Mutagenesis* 25:149–154
13. Feng Y, Li S, Li D, Wang Q, Ning P, Chen M, Tian X, Wang X (2018) Rational design of a diaminomaleonitrile-based mitochondria-targeted two-photon fluorescent probe for hypochlorite in vivo: solvent-independent and high selectivity over Cu^{2+} . *Sens Actuators B* 254:282–290
14. Liu XM, Qi YT, Pu SH, Wang Y, Gao ZQ (2021) Sensing mechanism of a new fluorescent probe for hydrogen sulfide: photoinduced electron transfer and invalidity of excited-state intramolecular proton transfer. *RSC Adv* 11:22214–22220
15. Feng H, Meng Q, Wang Y, Duan C, Wang C, Jia H, Zhang Z, Zhang R (2018) Responsive Fluorescence Probe for Selective and Sensitive Detection of Hypochlorous Acid in Live Cells and Animals. *Chem Asian J* 13: 2611–2618
16. Li P, Wang J, Wang X, Ding Q, Bai X, Zhang Y, Su D, Zhang W, Tang B (2019) In situ visualization of ozone in the brains of mice with depression phenotypes by using a new near-infrared fluorescence probe. *Chem Sci* 10:2805–2810
17. Liu XM, Wang Y, Wang YX, Tao YP, Fei X, Tian J, Hou YM (2021) Solvent effect on the excited-state intramolecular double proton transfer of 1,3-bis(2-pyridylimino)-4,7-dihydroxyisoindole. *Photochemical & Photobiological Sciences* 20: 1183–1194
18. Tang Z, Wang Y, Bao DS, Lv MH, Yang Y, Tian J, Dong L (2017) Theoretical Investigation of Excited-State Intramolecular Proton Transfer Mechanism for an Asymmetric Structure of 3,7-Dihydroxy-4-oxo-2-phenyl-4H-chromene-8-carbaldehyde: Single or Double? *J. Phys Chem A* 121: 8807-8814
19. Zhao JF, Chen JS, Cui YL, Wang J, Xia LX, Dai YM, Song P, Ma FC (2015) A questionable excited-state double-proton transfer mechanism for 3-hydroxyisoquinoline. *Phys Chem Chem Phys* 17:1142-1150
20. Tang Z, Zhou PW (2020) New Insights into the Excited State Dynamics of Quinoline–Pyrazole Isomerism. *J Phys Chem B* 124:3400-3407
21. Ren MG, Li ZH, Nie J, Wang L, Lin WY (2018) A photocaged fluorescent probe for imaging hypochlorous acid in lysosomes. *Chem Commun* 54:9238
22. Chen X, Wang F, Hyun JY, Wei T, Qiang J, Ren X, Shin I, Yoon J (2016) Recent progress in the development of fluorescent, luminescent and colorimetric probes for detection of reactive oxygen

- and nitrogen species. *Chem Soc Rev* 45:2976–3016
23. Liu YJ, Tian FF, Fan XY, Jiang FL, Liu Y (2017) Fabrication of an acylhydrazone based fluorescence probe for Al³⁺. *Sensors Actuators B Chem* 240: 916-925
 24. Chen X, Wang X, Wang S, Shi W, Wang K, Ma H (2008) A highly selective and sensitive fluorescence probe for the hypochlorite anion. *Chem Eur J* 14: 4719–24
 25. Ren HX, Huo FJ, Yin CX (2021) An ESIPT-based colorimetric and fluorescent probe with large Stokes shift for the sensitive detection of hypochlorous acid and its bioimaging in cells. *New J Chem* 45: 4724
 26. Pei GX, Dzade NY, Zhang Y, Hofmann JP, de Leeuw NH, Weckhuysen BM (2021) Identification of Photoexcited Electron Relaxation in a Cobalt Phosphide Modified Carbon Nitride Photocatalyst. *ChemPhotoChem* 330–334
 27. Thom KA, Förster T, Weingart O, Goto S, Takeda Y, Minakata S, Gilch P (2021) The Photophysics of Dibenzo[a,j]phenazine. *ChemPhotoChem* 335–347
 28. Frisch MJ, Trucks GW, Schlegel HB, Scuseria GE, Robb MA, Cheeseman JR, Scalmani G, Barone V, Petersson GA, Nakatsuji H, Li X, Caricato M, Marenich AV, Bloino J, Janesko BG, Gomperts R, Mennucci B, Hratchian HP, Ortiz JV, Izmaylov AF, Sonnenberg JL, Williams-Young D, Ding F, Lipparini F, Egidi F, Goings J, Peng B, Petrone A, Henderson T, Ranasinghe D, Zakrzewski VG, Gao J, Rega N, Zheng G, Liang W, Hada M, Ehara M, Toyota K, Fukuda R, Hasegawa J, Ishida M, Nakajima T, Honda Y, Kitao O, Nakai H, Vreven T, Throssell K, Montgomery JAJr, Peralta JE, Ogliaro F, Bearpark MJ, Heyd JJ, Brothers EN, Kudin KN, Staroverov VN, Keith TA, Kobayashi R, Normand J, Raghavachari K, Rendell AP, Burant JC, Iyengar SS, Tomasi J, Cossi M, Millam JM, Klene M, Adamo C, Cammi R, Ochterski JW, Martin RL, Morokuma K, Farkas O, Foresman JB, Fox DJ (2016) Gaussian 16, Revision C. 01, Wallingford CT
 29. Adamo C, Barone V (1999) Toward reliable density functional methods without adjustable parameters: The PBE0 model. *J Chem Phys* 110:6158–6169
 30. Grimme S, Antony J, Ehrlich S, Krieg H (2010) A consistent and accurate ab initio parametrization of density functional dispersion correction (DFT-D) for the 94 elements H-Pu. *J Chem Phys* 132:154104
 31. Schafer A, Horn H, Ahlrichs R (1992) Fully optimized contracted Gaussian basis sets for atoms Li to Kr. *J Chem Phys* 97:2571–2577
 32. Cancès E, Mennucci B, Tomasi J (1999) A new integral equation formalism for the polarizable continuum model: Theoretical background and applications to isotropic and anisotropic dielectrics. *J Chem Phys* 107:3032–3041
 33. Miertuš S, Scrocco E, Tomasi J (1981) Electrostatic Interaction of a Solute with a Continuum - A Direct Utilization of Ab initio Molecular Potentials for the Prediction of solvent Effect. *Chem Phys* 55:117–129
 34. Cammi R, Tomasi J (1995) Remarks on the Use of the Apparent Surface-Charges (ASC) Methods in Solvation Problems – Iterative Versus Matrix-Inversion of the Apparent Charges. *J Comput Chem* 16:1449–1458

35. Lu T, Chen FW (2012) Multiwfn: a multifunctional wavefunction analyzer. *J Comput Chem* 33: 580–592
36. Garcia JC, Johnson ER, Keinan S, Chaudret R, Piquemal JP, Beratan DN, Yang WT (2011) NCIPLLOT: a program for plotting non-covalent interaction regions. *J Chem Theory Comput* 7:625–632
37. Johnson ER, Keinan S, Mori-Sanchez P, Contreras-Carcia J, Cohen AJ, Yang WT (2010) Revealing noncovalent interactions. *J Am Chem Soc* 132: 6498–6506

Scheme 1

Scheme 1 is available in Supplemental Files section.

Figures

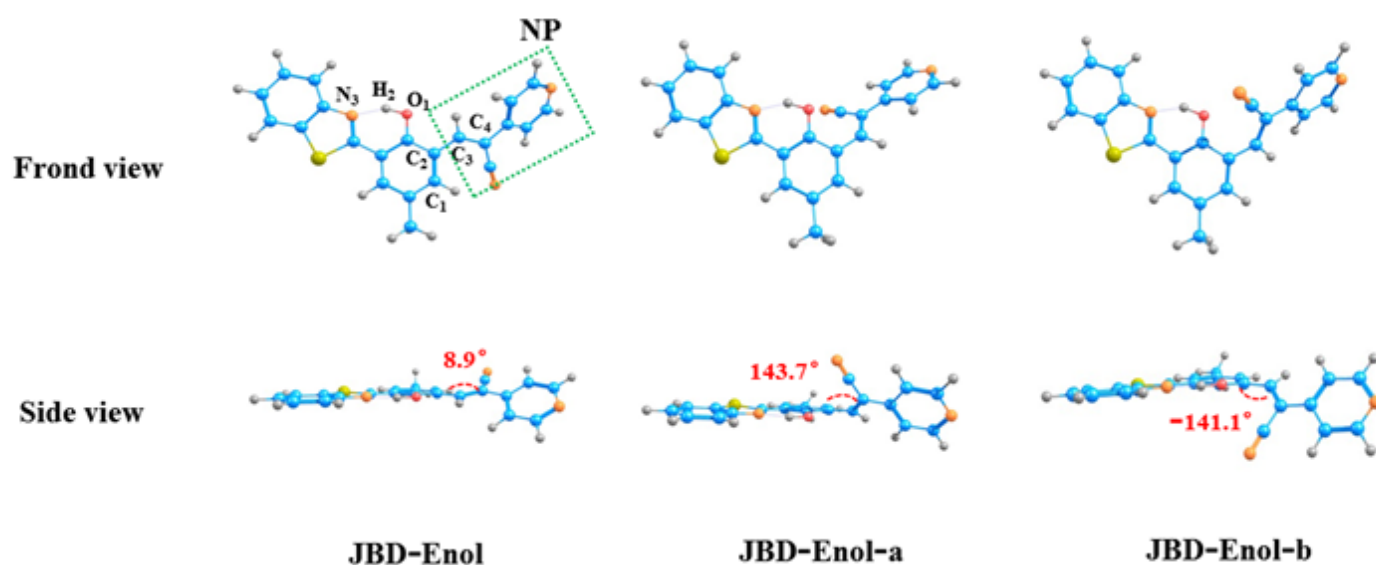


Figure 1

Optimized geometries of JBD-Enol, JBD-Enol-a, and JBD-Enol-b in the S_0 state based on PBE0/TZVP level.

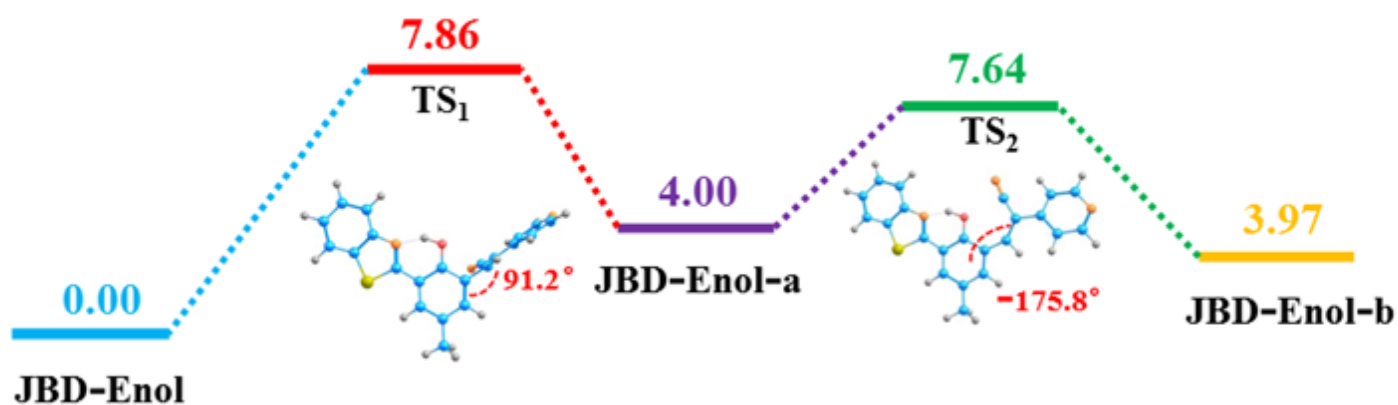


Figure 2

Energy barriers for the torsion of the $C_1C_2C_3C_4$ dihedral in the ground state (energies are given in kcal/mol).

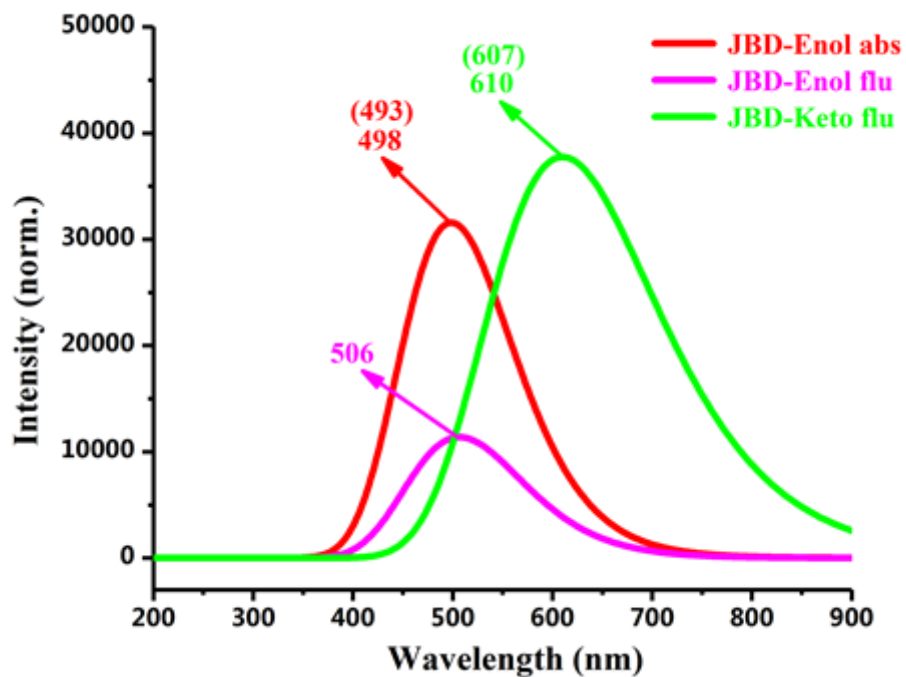


Figure 3

Theoretical absorption and fluorescence humps for the JBD in the ACN/H₂O solvent using the PBE0/TZVP method.

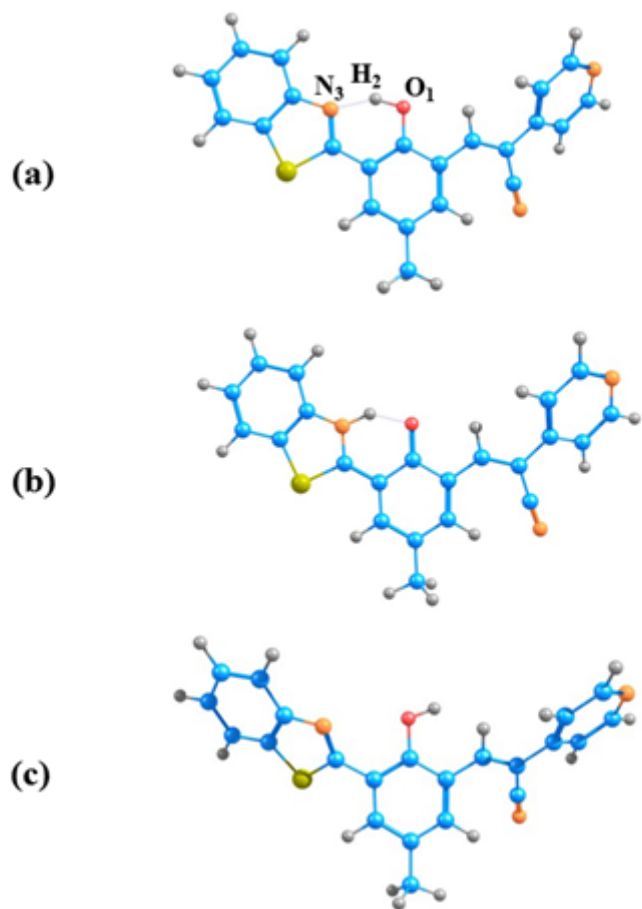


Figure 4

The optimized structures of JBD normal form (a), JBD tautomeric form (b) and JBD open form (c); red: O; gray: H; orange: N; blue: C; yellow: S.

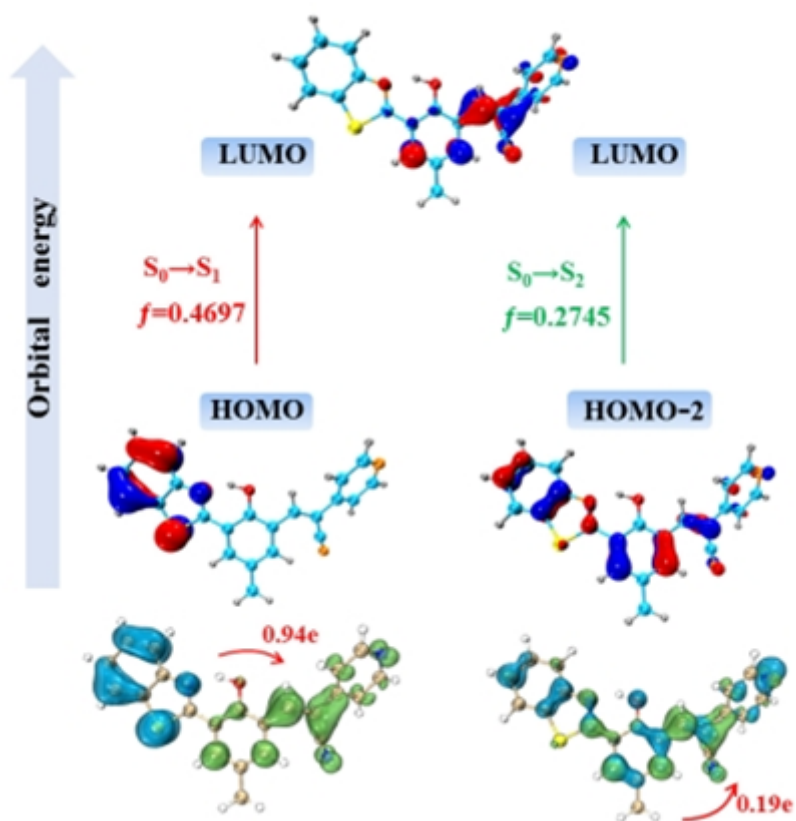


Figure 5

Excitation processes of probe JBD-Enol in the ACN/H₂O solvent (Molecular orbitals are given in blue and red iso-surfaces, holes are given in blue iso-surfaces and electrons are given in green iso-surfaces).

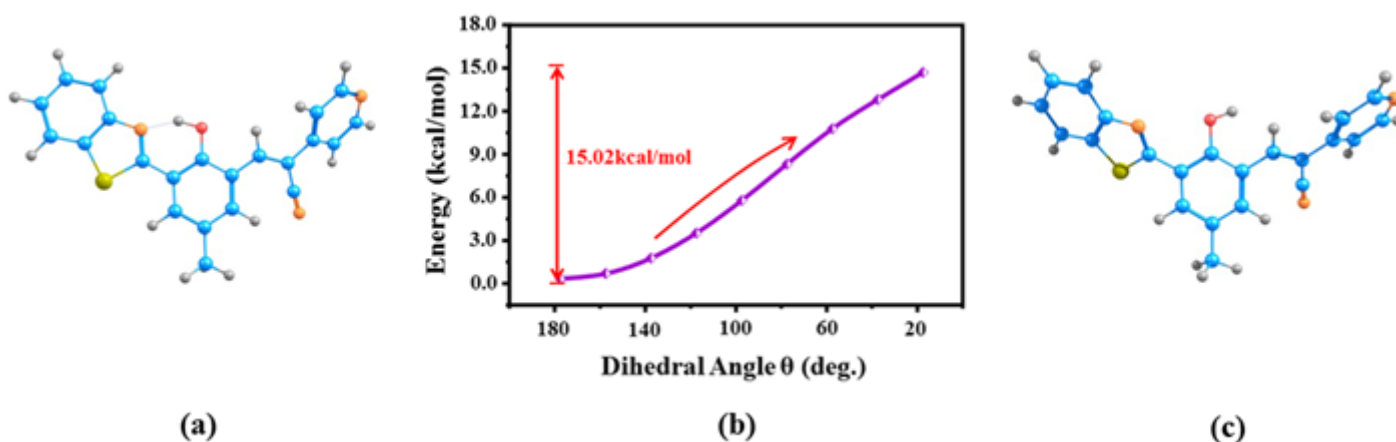


Figure 6

(a) Geometry of JBD-Enol in S_0 state; (b) Variation of energy as a function of rotation of the torsional angle (θ) for transformation of the intramolecular hydrogen bonded JBD-Enol form to the non-hydrogen

bonded JBD-open form as obtained at the PBE0/TZVP level; (c) Geometry of the JBD-open in S_0 state.

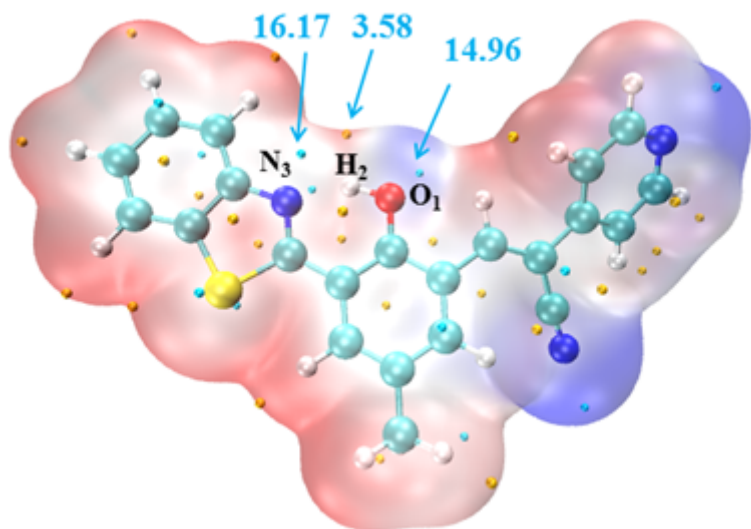
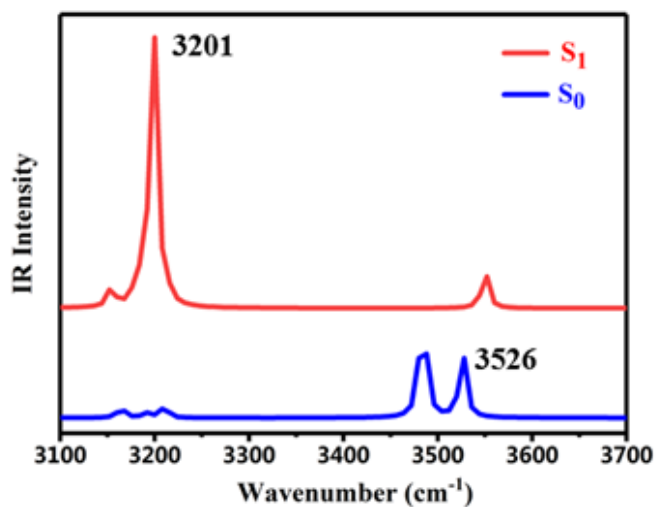
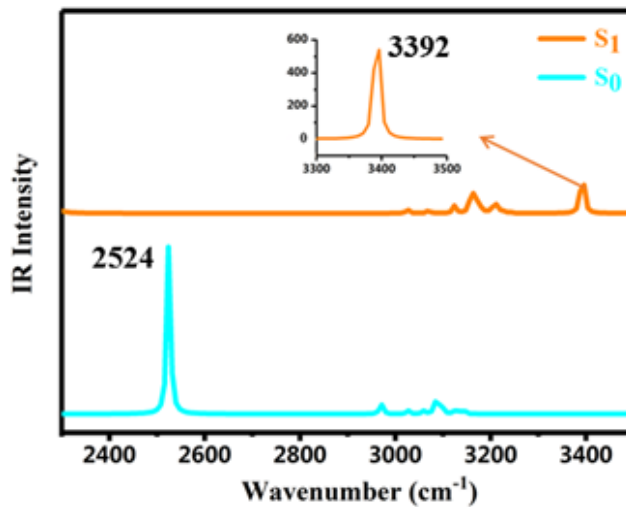


Figure 7

The total electron density isosurface mapped with molecular electrostatic potential surface (MEPS) for the JBD-Enol form.



(a)



(b)

Figure 8

Calculated IR spectra of JBD in the relevant spectral of O_1-H_2 (a) and H_2-N_3 (b) stretching band in the S_0 and S_1 states for JBD-Enol and JBD-Keto based on the PBE0/TZVP/IEFPCM theoretical level, respectively.

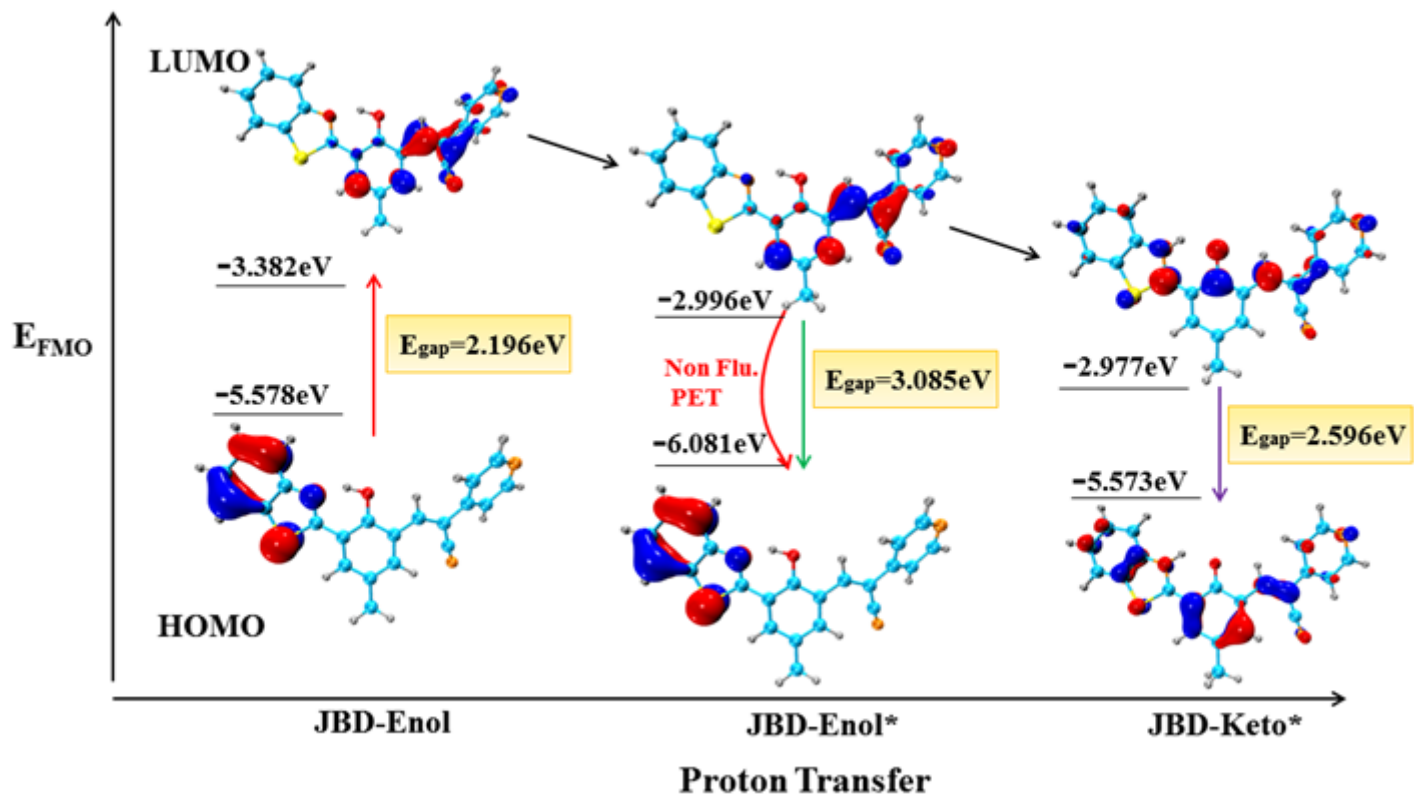


Figure 9

FMOs of probe JBD for S_0 and S_1 states (JBD-Enol), and S_1 state (JBD-Keto).

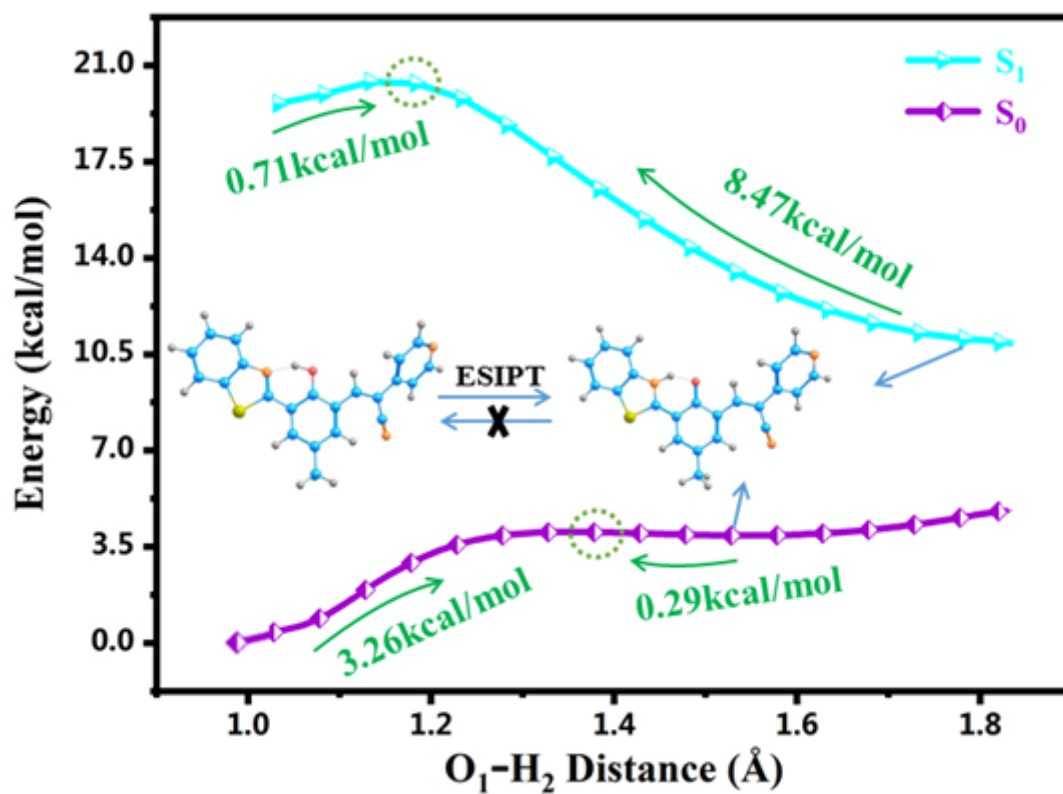


Figure 10

Potential energy curves of the ground and excited states for the probe JBD.

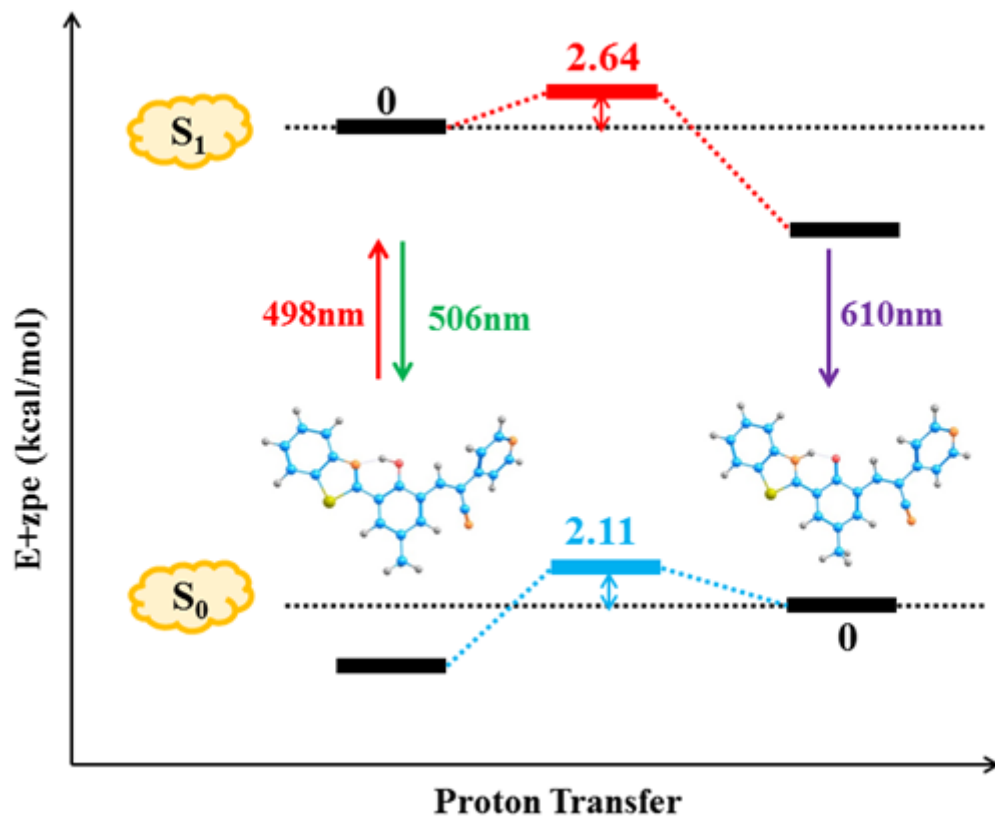


Figure 11

Sum of electronic and zero-point energies profiles of JBD-Enol, JBD-Keto, and the TS in S_0 and S_1 states.

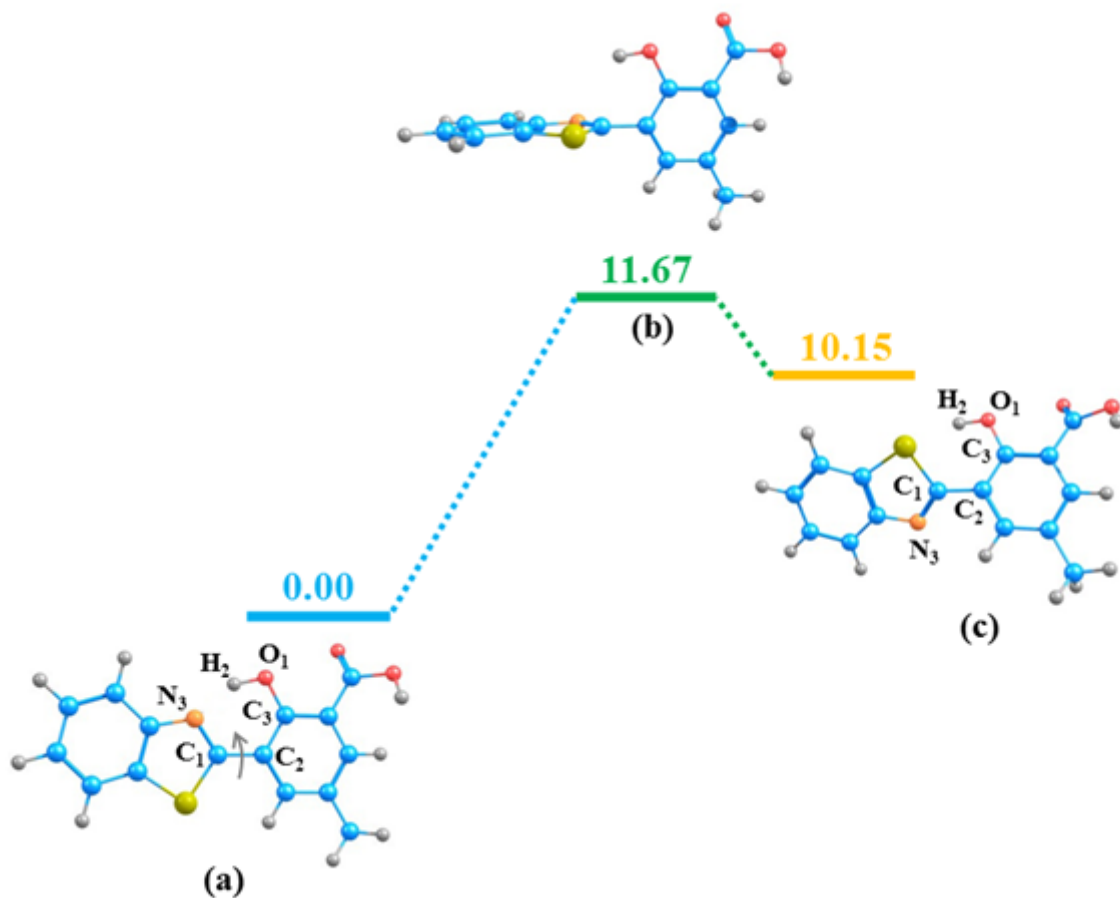


Figure 12

(a) The structure of HBT-COOH-a; (b) Energy barrier and transition state for the torsion of the $N_3C_1C_2C_3$ dihedral in the ground state (energies are given in kcal/mol); (c) The structure of HBT-COOH-b.

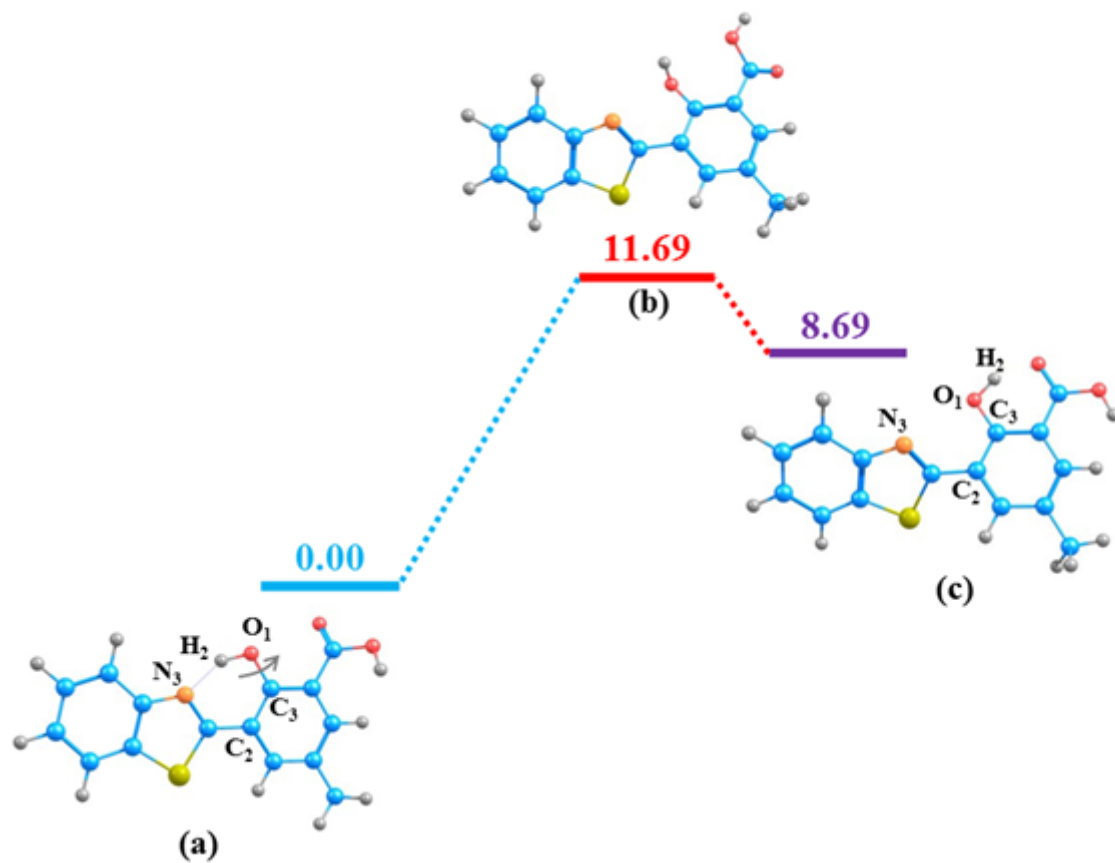
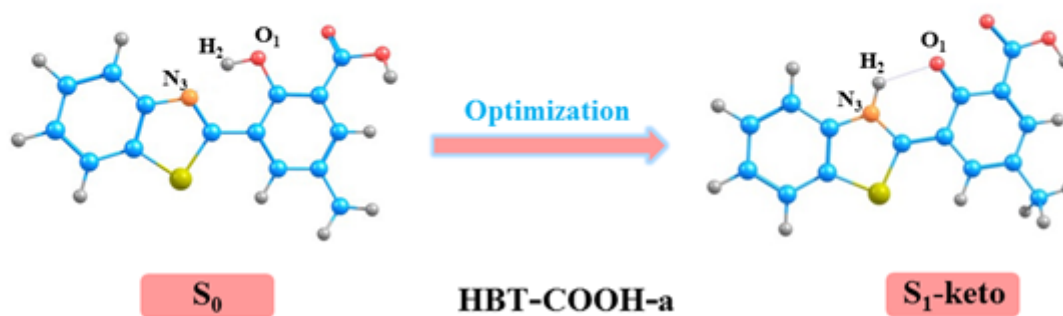


Figure 13

(a) The structure of HBT-COOH-a; (b) Energy barrier and transition state for the torsion of the $C_2C_3O_1H_2$ dihedral in the ground state (energies are given in kcal/mol); (c) The structure of HBT-COOH-c.

A**B**

HBT-COOH-a	S_0	S_1 -keto
O_1 - H_2	1.024	1.992
H_2 - N_3	1.621	1.019
$\delta(O_1$ - H_2 - $N_3)$	150.3	123.3

Figure 14

A: Optimization process from the S_0 state structure to the S_1 state structure of HBT-COOH-a; B: Calculated important bond lengths (\AA) and bond angles ($^\circ$) for the optimized structure of HBT-COOH-a in ground-state (S_0) and excited-state (S_1).

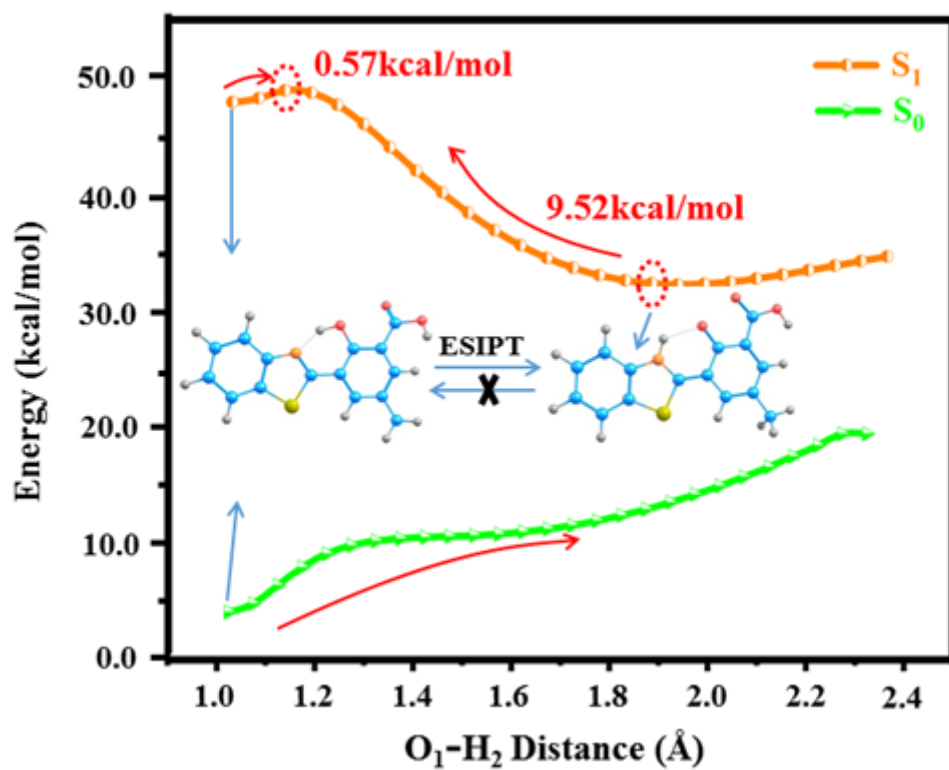


Figure 15

Potential energy curves of the S_0 and S_1 states for the HBT-COOH-a.

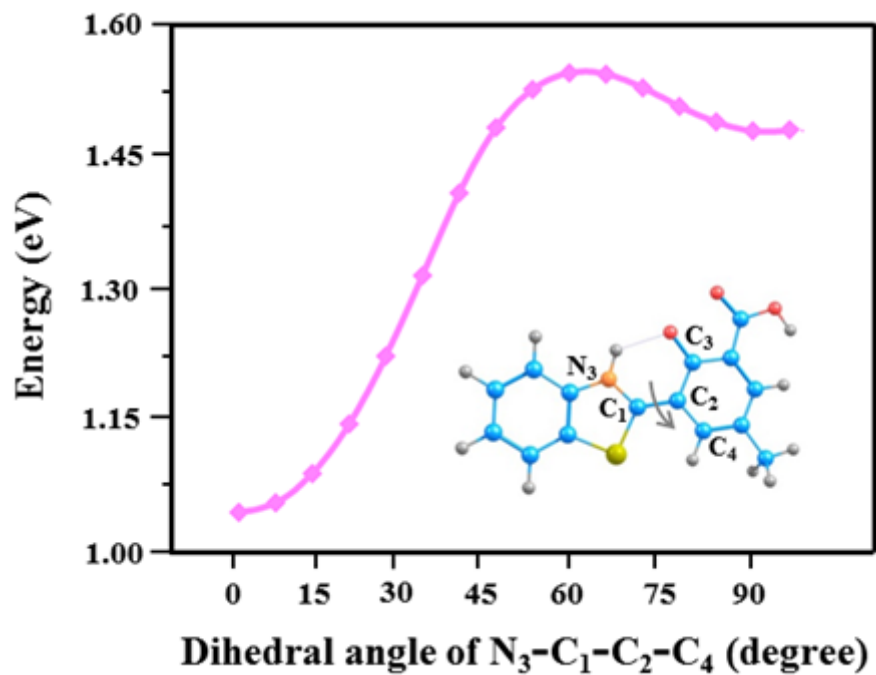


Figure 16

Variation of energy as a function of rotation of the dihedral angle of N₃-C₁-C₂-C₄ (degree) for transformation of the HBT-COOH-a (S₁) as obtained at the PBE0/TZVP level.

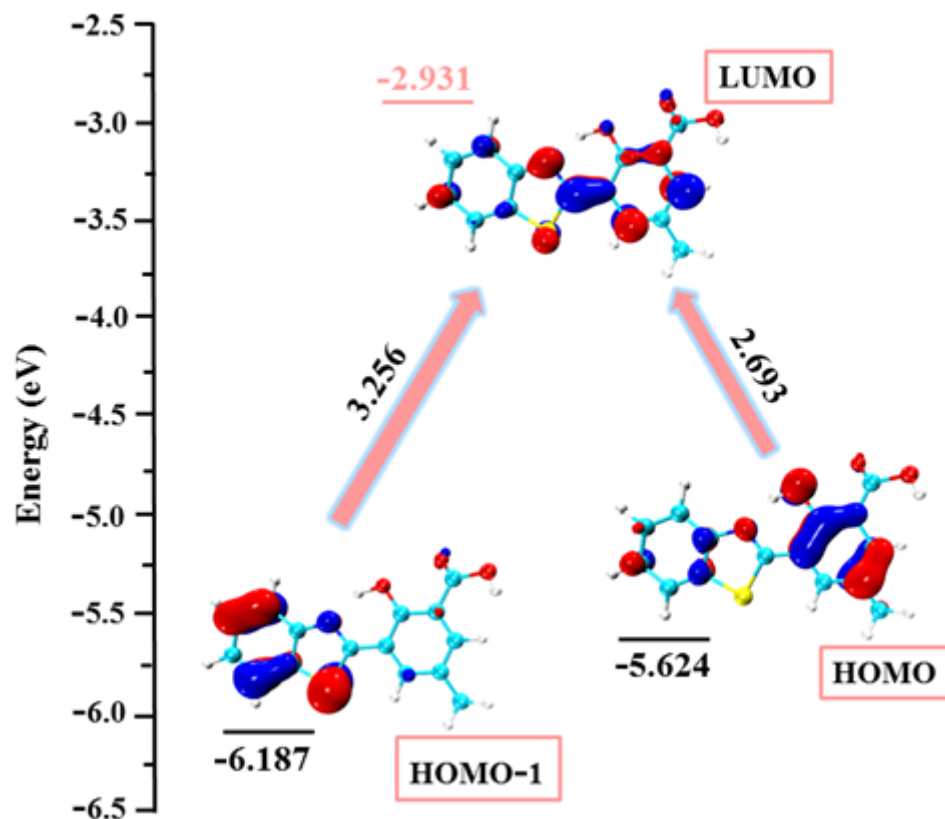


Figure 17

The frontier molecular orbitals of HBT-COOH-a.

Supplementary Files

This is a list of supplementary files associated with this preprint. Click to download.

- [GraphicalAbstract.doc](#)
- [Scheme1.png](#)